Nanoscale Advances

ROYAL SOCIETY OF CHEMISTRY

PAPER

View Article Online
View Journal | View Issue



Cite this: *Nanoscale Adv.*, 2025, **7**, 7028

# Synergistic catalytic and antibacterial activity, along with *in silico* molecular docking of bimetallic silver-copper-doped PVP-$Mg(OH)_2$ nanostructures

Zarqa Altaf,[a] Muhammad Imran,*[a] Ali Haider,*[b] Iram Shahzadi,[c] Zernab Mateen,[d] Anwar Ul-Hamid,[e] Ahmed M. Fouda[f] and Muhammad Ikram[d]

Received 18th July 2025
Accepted 12th September 2025

DOI: 10.1039/d5na00693g

rsc.li/nanoscale-advances

Industrial wastewater treatment is a critical challenge requiring innovative solutions to address global water scarcity. In this work, magnesium hydroxide $Mg(OH)_2$ nanostructures (NSs) were successfully synthesized *via* a cost-effective and sustainable co-precipitation approach, doped with 3 wt% polyvinylpyrrolidone (PVP) and varying amounts (2 and 4 wt%) of silver–copper (Ag–Cu). The main purpose of this research was to investigate the ternary system's ability in dye degradation and its antibacterial properties. PVP, as a capping agent, regulates the growth of the NSs and provides stability. The incorporation of Ag–Cu minimizes agglomeration and promotes the formation of a network comprising PVP-capped NSs along with Ag–Cu nanoparticles (NPs). This interconnected network facilitates charge transport, thereby enhancing the overall catalytic performance. The study revealed that 4 wt% Ag–Cu/PVP-$Mg(OH)_2$ significantly degrades (99.68%) rhodamine B (RhB) in acidic medium as opposed to alkaline and neutral pH levels, and it achieves a maximum inhibition zone of 7.95 ± 0.02 mm against MDR *Staphylococcus aureus* (*S. aureus*). The prospective inhibitory mechanism of the synthesized NSs on the DNA gyrase enzyme of *S. aureus* was explored by molecular docking.



## 1. Introduction

Water pollution has developed into a major problem and has increased drastically, thereby posing a global hazard to the existence of human beings and other forms of life.[1] In textiles, leather, and food manufacturing, rhodamine B (RhB) is extensively used. It is a hazardous carcinogen and mutagen that poses grave dangers to life forms.[2] Its existence in aquatic environments is highly detrimental to aquatic plant health due to its ability to block sunlight, thereby hindering photosynthesis and interrupting natural water purification processes. In addition, there have been various physical, chemical, and biological treatment methods, as well as UV-light-based techniques, used for the remediation of water pollutants.[3,4] Some conventional techniques are used to remove pollutants from wastewater, such as ion exchange, membrane filtration, chemical coagulation, electrolysis, reverse osmosis (RO), carbon filter, biological methods, and co-precipitation.[5] However, these techniques have limitations, as they consume large amounts of energy and are costly.

The catalytic technique was employed owing to its various advantages; this method is gaining more attention from researchers for the purification of wastewater. This technique involves the degradation of dye with the help of reducing agent $NaBH_4$ and nanocatalysts (NCs) in the absence of light. Both $NaBH_4$ and NCs reduce the energy barrier and accelerate the reaction kinetics, thereby facilitating efficient dye degradation.[6–8] Metal hydroxides have emerged as a potential candidate for wastewater treatment, attributed to their reusability and stability.[9–12] Among them, $Mg(OH)_2$ stands out as a promising candidate for environmental remediation, as it serves as both a dye degrader and antibacterial agent, attributed to its environmentally benign, nontoxic, noncorrosive, and biodegradable nature in conjunction with having a large surface area. The presence of a large amount of OH groups and its morphology significantly enhance the catalytic activity by facilitating charge movement, band gap engineering, and surface reactivity.[9,13,14] Moreover, its low weight, high stiffness, shielding capability, insulating behavior, and band gap energy make it a promising candidate for multiple applications.[15,16]

[a]*Department of Chemistry, Government College University, Faisalabad, Pakpattan Road, Sahiwal, Punjab, 57000, Pakistan. E-mail: dr.muhammadikram@gcu.edu.pk*
[b]*Department of Clinical Sciences, Faculty of Veterinary and Animal Sciences, Muhammad Nawaz Shareef, University of Agriculture, Multan 66000, Punjab, Pakistan*
[c]*School of Pharmacy, University of Management and Technology, Lahore, 54770, Pakistan*
[d]*Solar Cell Applications Research Lab, Department of Physics, Government College University Lahore, Lahore 54000, Punjab, Pakistan*
[e]*Core Research Facilities, Research Institute, King Fahd University of Petroleum & Minerals, Dhahran 31261, Saudi Arabia*
[f]*Chemistry Department, Faculty of Science, King Khalid University, P. O. Box 9004, Abha, 61413, Saudi Arabia*

Several synthesis routes have been employed to synthesize $Mg(OH)_2$, including sol–gel, microwave, solvothermal, and co-precipitation.[17] Co-precipitation is an eco-friendly, cost-effective, and widely employed route, as it enables control over size, morphology, and surface area by controlling temperature, pH, concentration, and reagents. This route has been used previously to synthesize $Mg(OH)_2$ with multiple morphologies, including hexagonal plates, tubes, and needle-like rods.[18] One study has demonstrated polymer-metal hydroxide nanocomposites that exhibit high degradation efficacy, enhanced light absorption ability, and easy post-recovery treatment.[17]

PVP has garnered significant interest owing to its hydrophilic nature, mechanical stability, biocompatibility, biodegradability, and transparency in the visible region. It is widely used as an effective surfactant for controlling the particle size, shape, and crystal facets. PVP also enhances the adsorption capacity of materials by increasing the surface area.[19,20] PVP inclusion has led to the formation of integrated and less hazardous nanocomposites. The hydroxyl and carbonyl groups in PVP render it an optimal capping agent, promoting strong interactions with the host material, yielding a stable, water-insoluble material. Furthermore, the surface OH groups of these nanocomposites can effectively engage with water-soluble contaminants, thereby augmenting their vulnerability to photocatalytic oxidation mechanisms.[6,17,21,22]

Apart from this fact, one of the methods that has received recent attention from researchers is the doping of metal oxides with metals like Ag, Cu, Au, and Mn.[23] Metals are an effective dopant, as the ionic radius of $Cu^{2+}$ closely matches that of $Mg^{2+}$; also, doping enhances the material's catalytic activity.[24,25] Silver nanoparticles (Ag-NPs) have emerged as promising materials for dye degradation and antimicrobial applications due to its high surface area and low toxicity. Ag has excellent catalytic potential and biocompatibility, making it an optimal choice as dopant for dye degradation and antibacterial application.[26–28] Copper nanoparticles (Cu NPs) show superior optical, electrical, and mechanical properties, and they demonstrate significant catalytic potential, attributed to a high surface-to-volume ratio and electrical conductivity.[29–31] Studies reported the ability of biogenic Ag@Cu alloy NPs in degrading dye *via* photocatalysis; they also exhibit antioxidant behavior.[32] Likewise, another study presented Cu@Ag and Ag@Cu core–shell nanostructures using ethylene glycol and investigated their degrading potential against *p*-nitrophenol.[33]

The environmentally benign co-precipitation route has been employed to synthesize $Mg(OH)_2$ NSs doped with varying weight ratios of Ag–Cu and a fixed quantity of PVP for the removal of RhB dye and to inhibit bacterial growth. To evaluate the effect of dopants (Ag–Cu and PVP) on $Mg(OH)_2$ NSs, a comprehensive investigation of their structural and optical properties was conducted, and its degrading efficacy against RhB dye was assessed. Subsequently, we evaluated their antibacterial efficacy against *Staphylococcus aureus*, and a credible mechanism for antibacterial action was predicted *via* a molecular docking study focused on DNA gyrase using ciprofloxacin as a reference. It was observed that the doping of different transition metals (Ag–Cu) into the host material $Mg(OH)_2$ enhanced the catalytic and antibacterial activities. PVP, as a capping agent, controls the size and enhances the stability of $Mg(OH)_2$, thereby increasing the catalytic and antibacterial behavior.

## 2. Experimental work

### 2.1. Materials

Magnesium chloride hexahydrate ($MgCl_2 \cdot 6H_2O \geq 98\%$), sodium hydroxide ($NaOH \geq 98\%$), silver nitrate ($AgNO_3 \geq 99\%$), copper chloride ($CuCl_2 \cdot 2H_2O \geq 99\%$), and PVP $(C_6H_9NO)_n$ were acquired from Sigma-Aldrich (Germany).

### 2.2. Synthesis of $Mg(OH)_2$ and doped $Mg(OH)_2$

$Mg(OH)_2$ was synthesized by dissolving the required amount of $MgCl_2 \cdot 6H_2O$ (0.5 M) into 50 mL deionized (DI) water (solution A). For PVP-$Mg(OH)_2$, a fixed (3 wt%) concentration of PVP was added to a solution of $MgCl_2 \cdot 6H_2O$ (solution B), as reported in our previous study.[34] Similarly, for Ag–Cu doped PVP-$Mg(OH)_2$ synthesis, 2 wt% of $AgNO_3$ and $CuCl_2$ (1 wt% of each) and 4 wt% of $AgNO_3$ and $CuCl_2$ (2 wt% of each) were added to the PVP-$MgCl_2$ solution, forming solution C and solution D, respectively. The solutions were kept under vigorous stirring and heating for 30 min at 80 °C. The solution pH was kept at ~12 by integrating 1 M NaOH dropwise while monitoring the pH of the solution using a pH meter. The colloidal solutions were then centrifuged twice at 6000 rpm for 6 min to remove impurities. The washed precipitates were dried overnight at 120 °C and pulverized to a fine powder (Fig. 1).

### 2.3. Segregation and identification of MDR *Staphylococcus aureus*

**2.3.1. Sample acquisition and identification.** A random selection of lactating cows clinically positive for mastitis was conducted at various marketplaces, veterinary clinics, and farms in the region (Punjab, Pakistan) for collection of specimens. Milk samples were gathered by directly milking from the cow into a sterile container, which was promptly transferred to the laboratory and stored at 4 °C. The obtained samples were then cultured onto mannitol salt agar, followed by incubation at 37 °C for 2 days. The preliminary identification of bacterial isolates was conducted *via* gram staining and biochemical assays.

**2.3.2. Antibiotic susceptibility assessment.** Antibiotic susceptibility of bacterial isolates was assessed *via* disc diffusion testing. Mueller–Hinton agar (MHA) plates were inoculated with 0.5 McFarland standard suspensions of *S. aureus*. Subsequently, microbicidal disks containing amoxicillin (5 μg), azithromycin (15 μg), ceftriaxone (30 μg), ciprofloxacin (5 μg), tetracycline (30 μg), gentamicin (10 μg), sulfamethoxazole + trimethoprim (23.75 μg + 1.25 μg), and imipenem (10 μg) were placed on the agar plates. To prevent potential overlap of inhibition zones, the disks were positioned at a measured distance. In accordance with the guidelines established by the National Committee for Clinical Laboratory Standards, MHA plates were incubated at 37 °C for 24 h, after which the zones of inhibitions (ZOI) were measured to identify antibiotic-resistant bacteria.

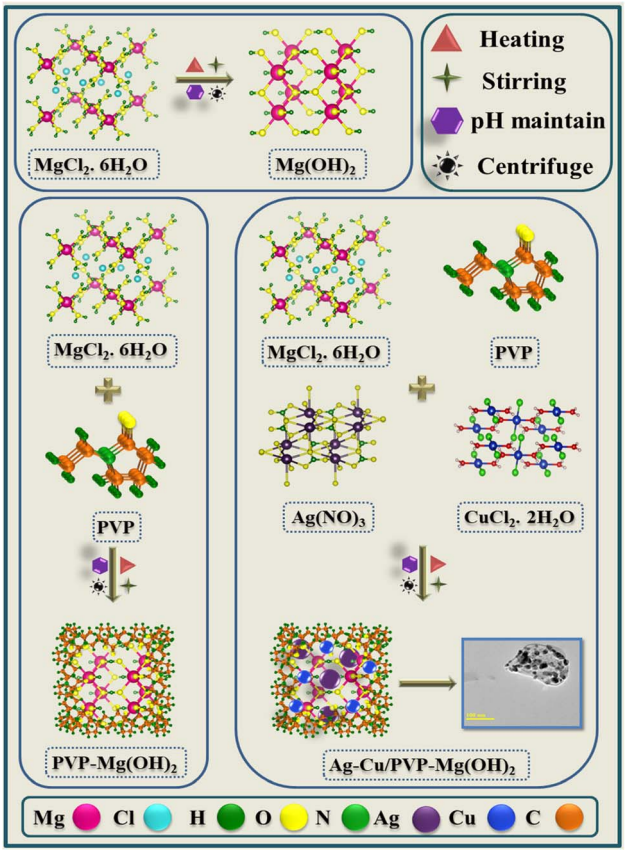


Fig. 1 Schematic diagram of the synthesis of $Mg(OH)_2$ and Ag–Cu doped PVP-$Mg(OH)_2$ NSs.

Bacteria revealing resistance to at least three antibiotics were classified as possessing multiple drug resistance (MDR).

**2.3.3. Antimicrobial activity.** The *in vitro* antibacterial potential of $Mg(OH)_2$ and doped $Mg(OH)_2$ NSs was assessed using the agar well diffusion method in triplicate. For this evaluation, ten representative isolates of MDR *S. aureus* were obtained from mastitis milk. Petri dishes of mannitol salt agar were swabbed with MDR *S. aureus* suspension equivalent to 0.5 McFarland standard. Wells of 6 mm diameter were generated through a sterile cork borer. $Mg(OH)_2$, PVP-doped $Mg(OH)_2$, and (2 and 4 wt%)Ag–Cu/PVP-doped $Mg(OH)_2$ NSs were introduced into the bore holes at low and high concentrations of 0.5 mg/50 μL and 1.0 mg/50 μL, respectively. Ciprofloxacin at a concentration of 0.005 mg/50 μL acted as the positive standard, while 50 μL of DI water served as the negative standard. Pristine and doped NS Petri dishes were incubated for 24 h at 37 °C. The inhibition areas (mm) were observed following incubation and calibrated at two perpendicular axes; subsequently, averages were noted using a digital vernier caliper by independent observers to reduce bias.

**2.3.4. Statistical analysis.** To evaluate the efficacy of pristine and doped NSs, the calibrated inhibition zone diameters (mm) were assessed and subjected to one-way ANOVA analysis using SPSS 24.0.[35]

### 2.4 Catalytic activity

The nanocatalyst degradation potential against RhB was investigated by conducting catalytic activity (CA) experiments in the absence of light, using $NaBH_4$ as a reducing agent and varying the pH of the dye solution. $H_2SO_4$ and NaOH were employed to obtain acidic and basic media, respectively. Freshly prepared $NaBH_4$ (400 μL) was added to 3 mL of RhB, and absorbance spectra were recorded using a UV-Vis spectrophotometer. Subsequently, 400 μL of synthesized catalyst was added to the solution of $NaBH_4$ and RhB. The results were monitored through UV-Vis spectra acquired at specified time intervals within the wavelength range of 200–800 nm.

### 2.5. Molecular docking analysis

The domains of structural biology and biomedicine have found extensive applications of computational molecular docking. This approach concentrates on atomic-level hydrophobic interactions, hydrogen bonds, and van der Waals forces, aiming to predict the interaction between ligands and target proteins (receptors). The bacterial DNA gyrase is crucial for maintaining the double helix structure and DNA replication. Therefore, investigating the DNA gyrase enzyme inhibitory effects of Ag–Cu/PVP-$Mg(OH)_2$ NSs were the focus of this study, with ciprofloxacin serving as a reference drug. Crystal structures of DNA gyrase were extracted from the protein data bank (ID: 5CPH).[36] To ensure structural validity and dependability of the protein models, the structures were geometrically optimized, solvent molecules were eliminated, and missing atoms were reinstated prior to docking. The energy reduction procedure was carried out utilizing the powell method, resulting in a convergence gradient of 0.05 kcal $(mol)^{-1}$ after 1000 cycles. After being tailored for the lowest energy conformations using the Tripos force field and Gasteiger Huckle force field, all ligand molecules were devised using the SYBYL-X 2.0 software.[37] Ultimately, all specified compounds underwent flexible docking into the active site of DNA gyrase using SYBYL-X 2.0.[38] The Surflex dock module utilizes a rigorously developed consensus scoring (cScore) function to assess and prioritize potential configurations of ligand fragments. This function integrates Hammerhead's empirical scoring mechanism, which entails a molecular similarity approach (morphological similarity) in conjunction with D-score (dock score), G-score (gold score), Chem-Score, potential mean force (PMF) score, and/or complete score.

## 3. Results and discussion

XRD patterns of the synthesized samples provide insights into crystal structure, crystallite size, and phase composition (Fig. 2a).[34] Diffraction peaks at 18.58°, 32.8°, 37.98°, 50.80°, 58.7° and 62.0° correspond to lattice planes (001), (010), (011), (012), (110) and (111), respectively, corroborated to the hexagonal phase of $Mg(OH)_2$, and synchronized with JCPDS card no. 96-900-6331. Braggs peaks positioned at 27.33°, 31.6°, and 56.41° correspond to reflection planes (210), (014), and (420), indicating the existence of monoclinic $Mg(CO)_3$ and well

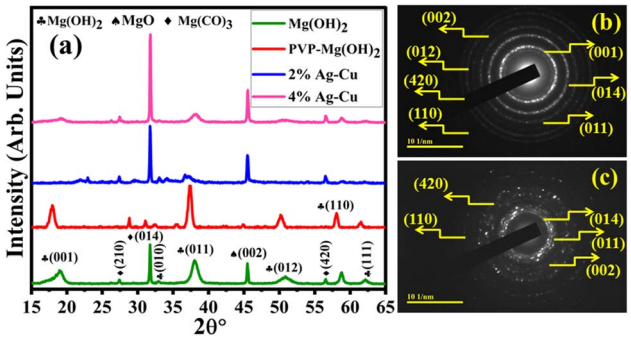


Fig. 2 (a) XRD diffractogram to evaluate the crystal structure of synthesized samples; (b and c) SAED analysis of (b) $Mg(OH)_2$ and (c) 4% Ag–Cu/PVP-$Mg(OH)_2$ NSs.

matching the index with JCPDS card no. 96-901-2798. An additional peak sited at 45.5 (002) corresponds to the cubic phase of MgO, synchronized with JCPDS card no. 96-901-3228. PVP's diffraction peak emerged at 28.8°, indicating its successful integration.[39] Moreover, the peaks analogous to lattice planes (001), (010), (011), (012), and (110) shifted towards lower angles, suggesting structural modifications in $Mg(OH)_2$ induced by PVP.[40] Ag–Cu addition resulted in the emergence of peaks at 23° and 34.0°, corresponding to lattice planes (021) and (002), confirming the formation of $Cu(OH)_2$ (JCPDS card no. 00-035-0505). At high concentration, no peak was observed for Ag–Cu, which might be due to the dispersion of small metal particles within the $Mg(OH)_2$ framework. The smaller size of Cu relative to Ag enhances its integration within the $Mg(OH)_2$ matrix. Furthermore, a shift in facets (010), (011), (211), and (110) was observed towards a higher angle with Ag–Cu, indicating interaction between Ag–Cu and PVP-$Mg(OH)_2$.[41,42] The increase in peak intensity indicates isotropic crystallite growth attributed to dopant-induced stable nucleation and the growth of larger crystallites.[43] The crystallite sizes of $Mg(OH)_2$, PVP-$Mg(OH)_2$, 2% Ag–Cu/PVP-$Mg(OH)_2$, and 4% Ag–Cu/PVP-$Mg(OH)_2$, computed using the Debye–Scherrer equation, were 29.35, 30.79, 39.69, and 51.6 nm, respectively. SAED patterns (Fig. 2b and c) revealed the polycrystalline nature of the $Mg(OH)_2$ and Ag–Cu/PVP-doped $Mg(OH)_2$. The bright circular rings with spots harmonized with the crystallographic facets of the XRD patterns.[34]

Vibrational mode and functional group evaluations of the prepared NSs were carried out *via* FTIR analysis of the spectra acquired in the wavenumber range of 3800–450 $cm^{-1}$ (Fig. 3a).[34] The sharp band at 3699 $cm^{-1}$ corresponds to the OH stretching vibrations, while the broad transmittance band ~3440 $cm^{-1}$ was associated with the stretching vibrations of water molecules.[44] The band observed ~2368 $cm^{-1}$ is ascribed to the characteristic C=O stretching mode originating from the adsorption of atmospheric $CO_2$.[45] The surface hydroxyl groups and adsorbed water molecules are manifested by the bands at 1442 $cm^{-1}$ and 1630 $cm^{-1}$, associated with Mg–OH and –OH group bending vibrations.[46] Bidentate carbonate forms on $Mg^{2+}$ cations, exhibiting asymmetric (O–C–O) stretching at 1528 $cm^{-1}$.[47] Furthermore, the bands at 829 and 538 $cm^{-1}$ were attributed to Mg–O stretching vibrations.[46,48] With PVP addition, two weak bands appeared at ~1075 and 1171 $cm^{-1}$, linked with the characteristic –CN stretching vibration of PVP.[49,50] Furthermore, a subtle shift in spectral bands towards a lower wavenumber was observed, verifying the interaction between $Mg(OH)_2$ and PVP or complexation of $Mg(OH)_2$ with the polymer blend.[51,52] The slight shift and variation in band intensity with Ag–Cu addition were attributed to its interaction within the PVP-$Mg(OH)_2$ lattice sites. The variation in intensity, ascribed to a change in the crystal radii of doped elements $Ag^{1+}$ (1.25 Å) and $Cu^{2+}$ (0.73 Å) compared to $Mg^{2+}$ (0.74 Å), significantly modifies the structure of the doped $Mg(OH)_2$.[53,54]

UV-Vis spectroscopy was employed to evaluate the optical properties and electronic structure of $Mg(OH)_2$ and Ag–Cu/PVP-$Mg(OH)_2$ (Fig. 3b). The absorbance spectrum of $Mg(OH)_2$ exhibits a peak absorption ~289 nm and an absorption hump within the range of 350 to 450 nm.[55,56] The addition of PVP shifts the absorption range towards higher wavelength. This red shift suggests the formation of a complex and interaction between the polymer and $Mg(OH)_2$.[17,51] The increase in the absorption range and shift in spectra result from electrostatic interaction, van der Waals interaction, and H-bonding between PVP and $Mg(OH)_2$.[57] The absorption is enhanced in the low photon energy region, with the increasing concentration of Ag–Cu in PVP-$Mg(OH)_2$.[58] The direct band gap energy ($E_g$) calculated from Tauc plots following the straight line equation was determined to be 3.5, 2.97, 2.84, and 2.67 eV for $Mg(OH)_2$, PVP-$Mg(OH)_2$, 2% Ag–Cu/PVP-$Mg(OH)_2$, and 4% Ag–Cu/PVP-$Mg(OH)_2$, respectively

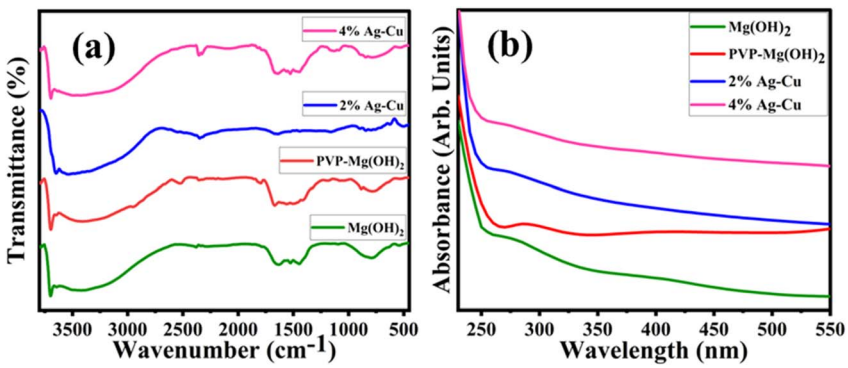


Fig. 3 (a) FTIR for functional group and vibrational mode analysis, and (b) absorbance spectra of $Mg(OH)_2$ and doped $Mg(OH)_2$ NSs.

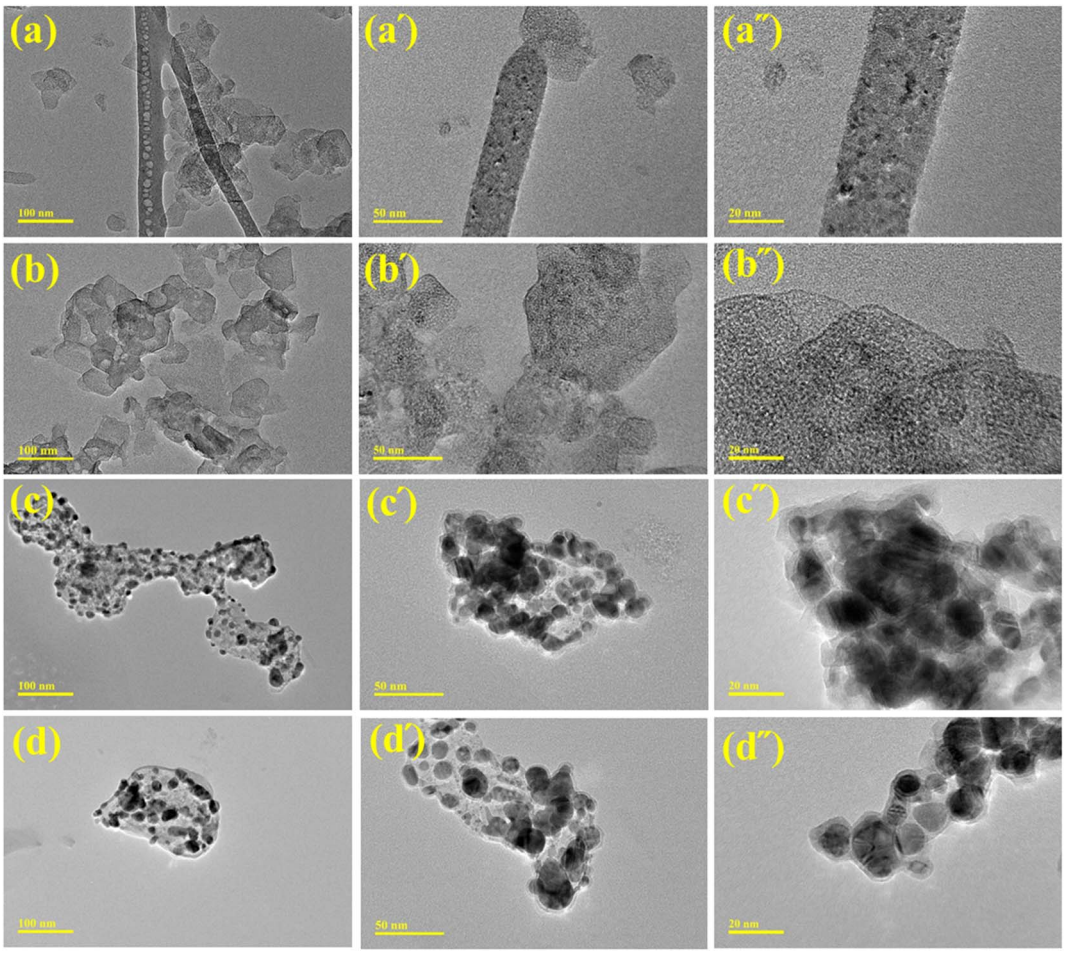


Fig. 4 TEM micrographs of (a–a″) $Mg(OH)_2$, (b–b″) PVP-$Mg(OH)_2$, (c–c″) 2 wt% Ag–Cu/PVP-$Mg(OH)_2$, and (d–d″) 4 wt% Ag–Cu/PVP-$Mg(OH)_2$ NSs at the different resolutions of 100 nm, 50 nm, and 20 nm, respectively.

(Fig. S1).[55] The formation of charge–transfer complexes (CTCs) due to the coordination bonds between $Mg^{2+}$ ions and PVP resulted in enhanced ionic conductivity, causing a decrease in $E_g$.[59] The addition of Ag–Cu generates new energy states, modifies its electronic structure, and improves photon absorption ability, thereby effectively lowering the $E_g$. This reduction in $E_g$ was attributed to the $Mg^{2+}$ substitution with $Cu^{2+}$ ions, as evidenced by XRD analysis.[60,61]

EDS analysis was carried out to scrutinize the elemental composition of 4% Ag–Cu/PVP-$Mg(OH)_2$ (Fig. S2). The presence of Mg, O, C, Ag, and Cu peaks validates the successful synthesis of Ag–Cu/PVP-$Mg(OH)_2$. The appearance of Au peaks in the EDS profile was attributed to spray coating intended to reduce the charging effect. Additionally, Na and Cl peaks emerged due to residual impurities, as NaOH was used to maintain the pH of solution and $MgCl_2$ and $CuCl_2$ were used as Mg and Cu precursors during synthesis. Elemental mapping was conducted to analyze the distribution of elements in the prepared sample (Fig. S3). Mapping analysis of the highly doped sample demonstrates the distribution of Mg, O, C, Na, Cl, Cu, Ag, and Au, represented with different colors.

The morphological and topographical aspects of undoped and doped $Mg(OH)_2$ were elucidated by TEM analysis (Fig. 4a–d″). Fig. 4a–a″ demonstrates the formation of interconnected nanoparticles embedded in nanorods and an agglomerated polygonal sheet of $Mg(OH)_2$.[34] The agglomeration of sheets might be due to the high surface energy of $Mg(OH)_2$ and hydrogen bonding between hydroxyls of the surface. The addition of PVP caused agglomeration, ascribed to hydrogen bonding with the OH group on the $Mg(OH)_2$ surface, stabilizing and capping the $Mg(OH)_2$ NSs. With Ag–Cu incorporation, uniform spheroid NPs composed of Ag and Cu, interconnected with $Mg(OH)_2$ sheets, were observed. The increasing concentration of Ag–Cu prevents agglomeration, forming an interconnected network of capped NSs (sheets and NPs of Ag–Cu) that improves the catalytic activity.

Gatan software was used to examine and ascertain the *d*-spacing of samples using HR-TEM micrographs having resolution of 5 nm. The interlayer *d* spacings of the control and PVP-, 2% Ag–Cu/PVP-, and 4% Ag–Cu/PVP-doped $Mg(OH)_2$ were found to be 0.23, 0.241, 0.237, and 0.247 nm (Fig. 5a–d), respectively, well synchronized with XRD results. Doping improves the crystallinity of the material, reducing structural

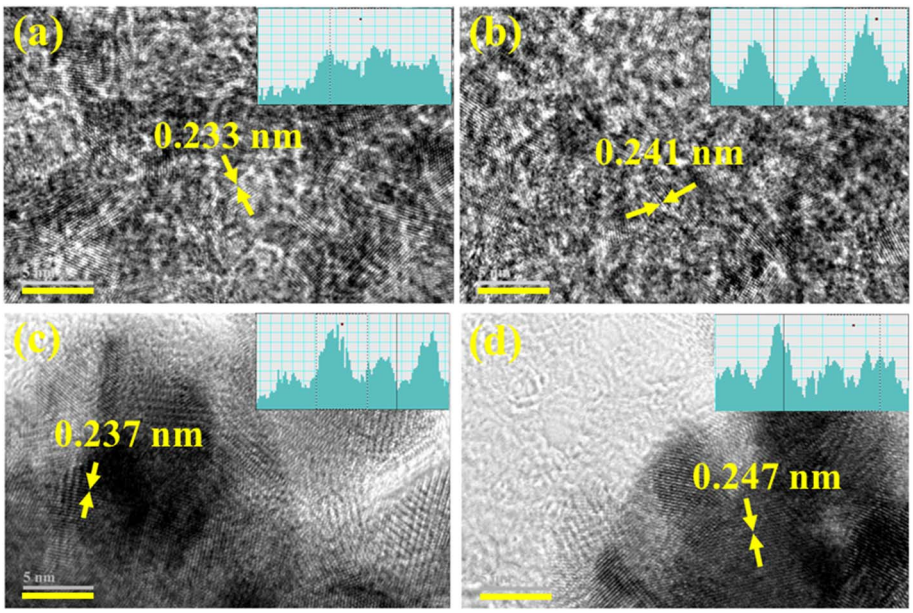


Fig. 5 (a–d) Calculated *d*-spacing of (a) $Mg(OH)_2$, (b) PVP-$Mg(OH)_2$, (c) 2 wt% Ag–Cu/PVP-$Mg(OH)_2$, and (d) 4 wt% Ag–Cu/PVP-$Mg(OH)_2$ NSs.

disorder and strain. By occupying lattice or interstitial sites, dopants stabilize the crystal structure, improve lattice ordering, and increase active sites, ultimately boosting the catalytic activity of NSs.

NCs coupled with $NaBH_4$ facilitate the degradation of RhB, as illustrated in Fig. S4. In the absence of NCs, there is a significant energy barrier between the reacting species, and $NaBH_4$ reacts slowly, slowing down the reaction kinetics. In

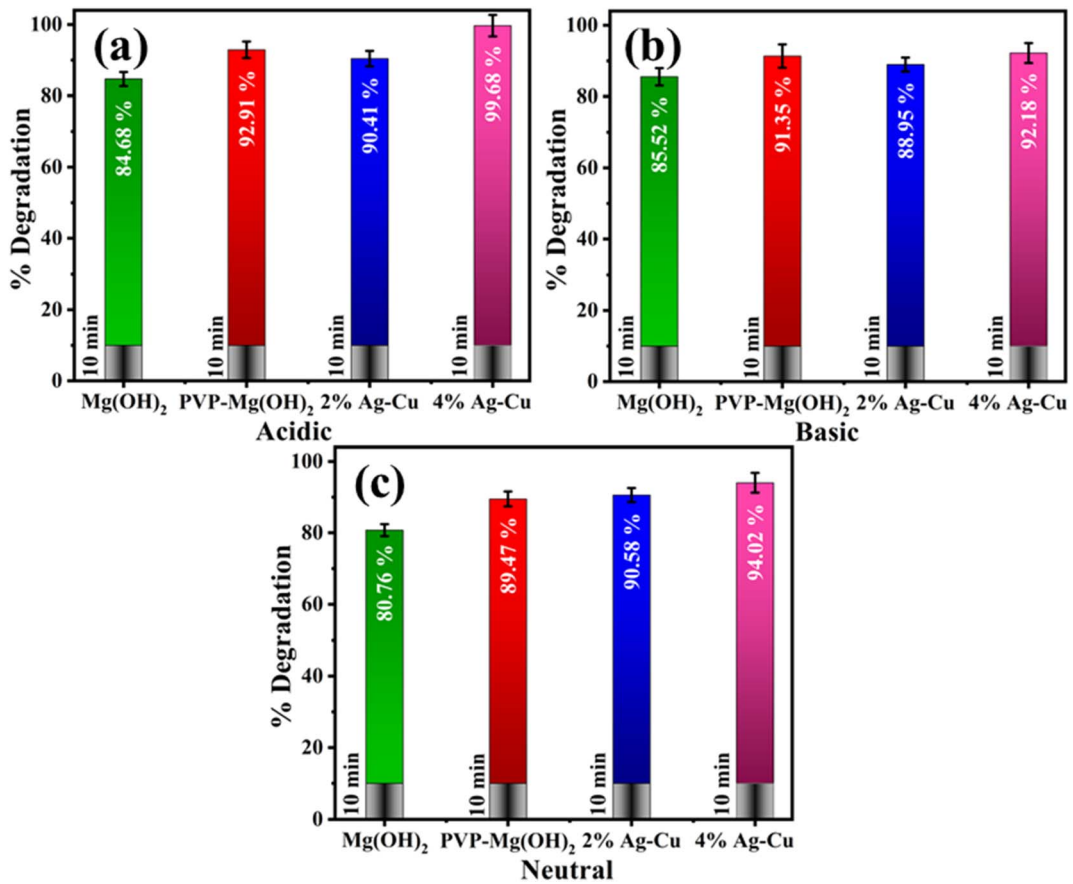


Fig. 6 RhB degradation using prepared NSs in (a) acidic, (b) basic, and (c) neutral media.

contrast, the addition of NCs accelerates the reaction kinetics by lowering the energy barrier through bridging the redox potential gap between $NaBH_4$ and RhB. NCs function as mediators and facilitate electron transfer, subsequently accelerating the reaction rate. During the reduction process, $NaBH_4$ dissociates into sodium ($Na^+$) and borohydride ions ($BH_4^-$). $BH_4^-$ electrostatically adsorbs on the surface of the NC and releases electrons to the catalyst, which splits $BH_4^-$ into hydrogen ions. The NCs channel electrons from the adsorbed $BH_4^-$ ions to RhB molecules. Following this electron transfer, the adjacent RhB molecules are attacked by the generated $H^+$, resulting in the breakdown of π-bonds within the chromophoric structure of RhB, converting it into leuco-RhB. Ag–Cu NPs act as electron reservoirs, accelerating electron transfer from $BH_4^-$ during the RhB reduction process.[8,62,63] The catalytic degradation potential of prepared NCs for RhB reduction was evaluated *via* UV-Vis spectrophotometer. The degradation efficacies of the $Mg(OH)_2$ and the PVP-, 2% Ag–Cu/PVP-, and 4% Ag–Cu/PVP-doped $Mg(OH)_2$ were found to be 86.68, 92.91, 90.41, and 99.68% in acidic media (pH = 4); 85.52, 91.35, 88.95, and 92.18% in alkaline media (pH = 12); and 80.76, 89.47, 90.58 and 94.02% in neutral media, respectively (Fig. 6a–c).

The control $Mg(OH)_2$ is known for its good catalytic properties but is limited in generating active sites for dye degradation, resulting in low efficiency as compared to doped $Mg(OH)_2$.[64] The addition of PVP serves as a surface stabilizer and can control the morphology of $Mg(OH)_2$, thereby increasing the available reaction surface area. This leads to higher degradation efficiency, since there will be more dye molecules interacting with the active sites at the surface of $Mg(OH)_2$.[65] Ag and Cu incorporation enhances catalytic activity through new active site formation, resulting in accelerated charge separation. However, the degradation efficiency drops, which might be due to suboptimal doping concentration. At this level, there may not be enough Ag–Cu to make an appreciable increment, or it may bring about charge carrier recombination, leading to low overall catalytic efficacy. Increasing the amount of dopant concentration (4% Ag–Cu) results in more active sites available for catalytic reactions and subsequently enhances the degradation efficiency.[8,42,66] The optimal catalytic performance occurs for $Mg(OH)_2$ with 4% Ag–Cu/PVP-$Mg(OH)_2$ in an acidic solution, resulting in 99.68% degradation within 10 minutes. RhB decolorization in the presence of $NaBH_4$ leads to the dye's reduction, as the synthesized materials act as electron-relaying systems through which $BH_4^-$ ions (donor) donate electrons to RhB (acceptor). Adsorption between $BH_4^-$ ions and dye molecules was made easier by the plentiful active sites on the catalyst.[67] Moreover, solution pH has also been found to affect the charge properties of the dye and catalysts in the degradation process.

The RhB structure contains a carboxylic group and an amino group. In acidic medium ($H_2SO_4$), the carboxylic group is in a protonated state. Catalytic activity increased in the acidic medium, ascribed to more $H^+$ ions produced for absorption by

Table 1 Antibacterial efficacy of Ag–Cu/PVP-$Mg(OH)_2$ NSs

| Sample | Inhibition zone (mm) (0.5 mg/50 μL) | Inhibition zone (mm) (1.0 mg/50 μL) | CIP (0.005 mg/50 μL) positive control | DI water (50 μL) negative control |
|---|---|---|---|---|
| $Mg(OH)_2$ | 0 ± 0.0 | 4.65 ± 0.04 | 8.45 ± 0.02 | 0 ± 0.0 |
| PVP-$Mg(OH)_2$ | 2.85 ± 0.05 | 5.35 ± 0.04 | 8.45 ± 0.02 | 0 ± 0.0 |
| 2% Ag–Cu | 4.75 ± 0.04 | 6.45 ± 0.03 | 8.45 ± 0.02 | 0 ± 0.0 |
| 4% Ag–Cu | 5.80 ± 0.04 | 7.95 ± 0.02 | 8.45 ± 0.02 | 0 ± 0.0 |

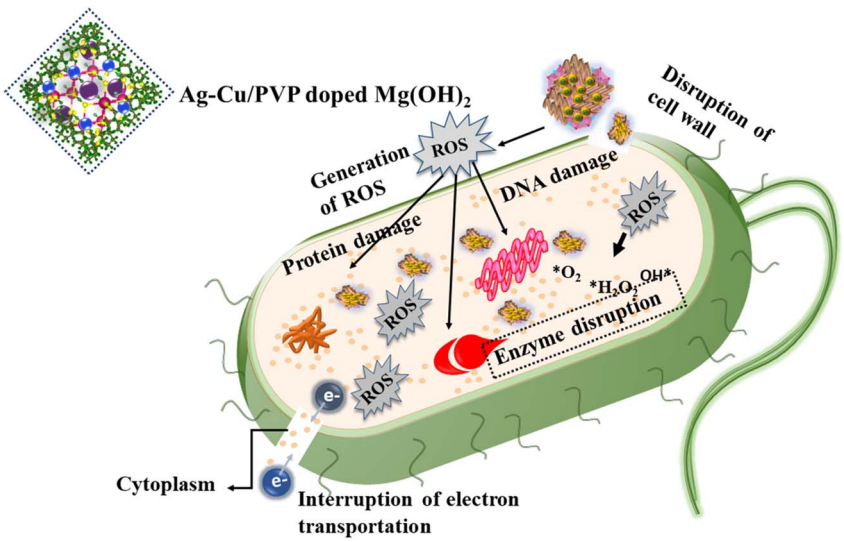


Fig. 7 Antibacterial activity of Ag–Cu/PVP doped $Mg(OH)_2$ NSs.

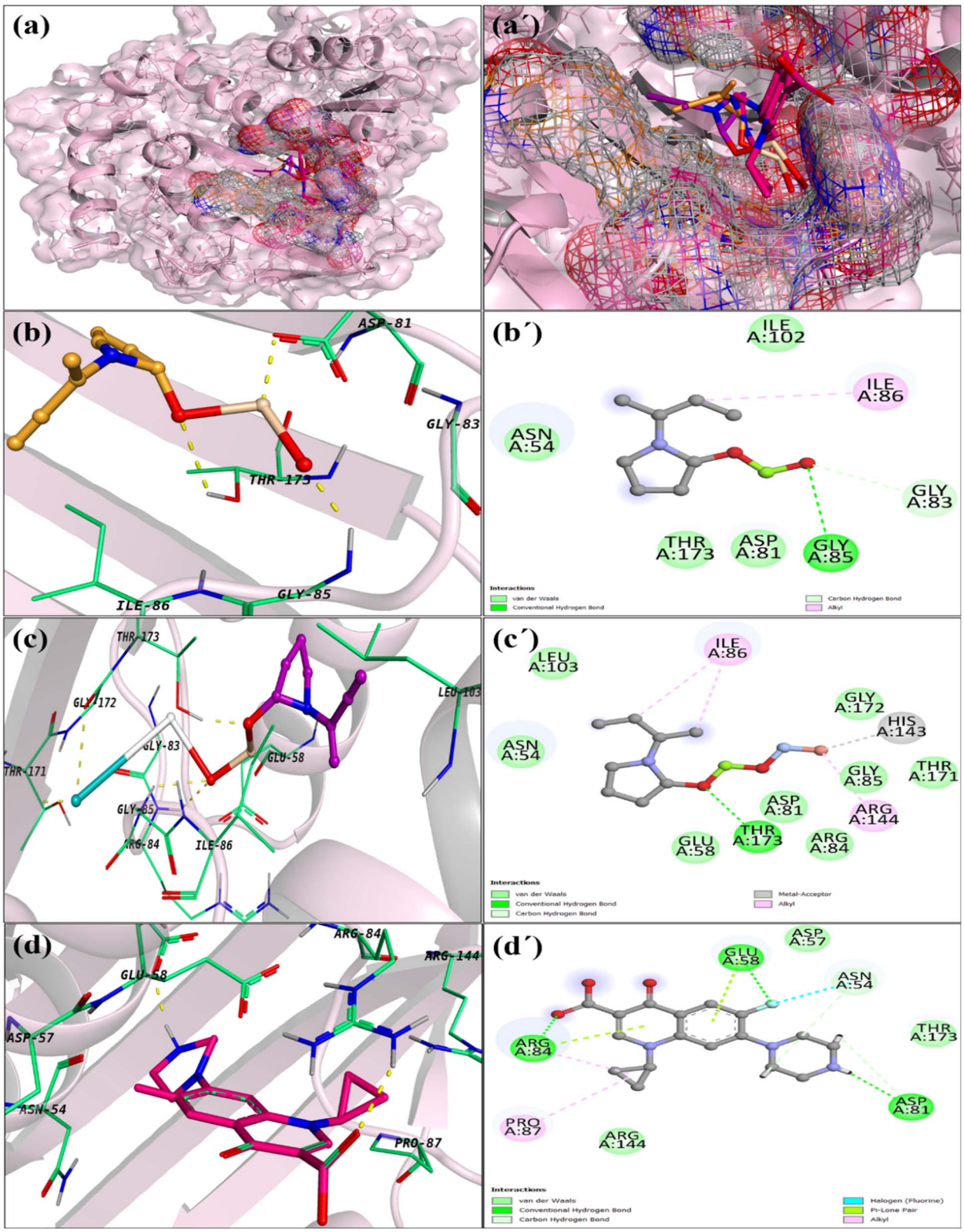


Fig. 8 (a and a′) Generated docked complexes of Ag–Cu/PVP-$Mg(OH)_2$ bonded to its corresponding molecular target DNA $gyrase_{S.\ aureus}$; 3D and 2D binding interaction perspectives of (b and b′) PVP-$Mg(OH)_2$, (c and c′) Ag–Cu/PVP-$Mg(OH)_2$, and (d and d′) ciprofloxacin within the active pocket of DNA gyrase. H-bonds are represented as yellow dotted lines.

the catalyst surface. The decolorization efficiency of RhB has risen with decreased solution pH due to greater electron transfer, redox potential, and catalyst surface charge density.[68] In basic medium, the concentration of hydroxyl groups is large, as NaOH is used to basify the solution. This large number of hydroxyl groups enhances RhB adsorption. In contrast, an excess of –OH groups oxidizes RhB, thereby reducing catalytic activity as compared to the acidic environment. At pH ~12, the generation of surface hydroxyl complexes hinders direct contact between the catalyst and dye. Additionally, a decrease in –OH adsorption leads to a lower generation of hydroxyl radicals. Consequently, at high pH, the efficiency of RhB degradation is less than at low pH.[69–71]

Table 1 and Fig. S5 summarize the *in vitro* antibacterial effectiveness of $Mg(OH)_2$, PVP-$Mg(OH)_2$, and Ag–Cu/PVP-$Mg(OH)_2$ against MDR *S. aureus.* Results depict inhibitory zone diameters ranging from 0 ± 0.0 to 5.80 ± 0.04 mm (low concentration) and 4.65 ± 0.04 to 7.95 ± 0.02 mm (high concentration) for MDR *S. aureus*. During calibration for MDR *S. aureus*, the negative control with DI Water indicated 0 ± 0.0 mm, and a +ve control, ciprofloxacin, presented 8.45 ± 0.02 mm inhibition region for MDR *S. aureus*. The 4% Ag–Cu/PVP-$Mg(OH)_2$ outperformed other prepared samples and demonstrated a significant inhibition zone of 7.95 ± 0.02 mm. The small size of NCs and increased number of active sites in Ag–Cu/PVP-$Mg(OH)_2$ facilitate effective penetration and destruction of bacteria (Fig. 7).

Bacterial $O_2$ is absorbed by vacant oxygen spaces on catalyst surfaces, resulting in the generation of ROS such as $OH^{\bullet}$, $O_2^{-\bullet}$, and $H_2O_2$. These ROS induce oxidative stress in bacterial cells, disrupting cellular components such as lipids, compromising membrane integrity, causing leakage of cellular contents, impairing respiration, and ultimately resulting in cell destruction. The direct contact of $Mg(OH)_2$ and the cell surface mechanically disrupts the bacterial cell wall. Additionally, moisture adsorbed on the $Mg(OH)_2$ surface forms an alkaline layer, which compromises the bacterial cell wall, causing cell death.[72,73] PVP addition enhances the antimicrobial effectiveness by improving the binding ability of $Mg(OH)_2$ to the cell wall. The cationic sites in PVP, coupled with hydroxyl groups, directly attach to the phospholipid bacterial membrane, compromising its integrity and resulting in leakage of cytoplasmic contents. PVP-$Mg(OH)_2$ can penetrate the cytoplasm more effectively, thereby boosting the antibacterial activity.[74] The addition of bimetallic components (Ag–Cu) in PVP-$Mg(OH)_2$ increases the antibacterial potential, attributed to the synergistic interaction between Ag and Cu. $Ag^+$ and $Cu^{+2}$ ions diffuse outward from the wells, penetrating bacterial cells, and are crucial in strengthening the activity of the NCs. This penetration of ions disturbs the cellular processes and effectively inhibits bacterial growth. Ag–Cu/PVP-$Mg(OH)_2$ generates excitons due to the electronic excitation from valence to conduction band. The electronic reaction with $O_2$ generates radicals ($O_2^{-\bullet}$), leading to the production of $H_2O_2$. The hole reacts with water molecules, forming $OH^{\bullet}$. These resulting ROS are pivotal, as they significantly contribute to the breakdown of lipids or protein molecules in the outer surface of bacteria.[75,76]

The *in silico* study offers profound insights into the structural and functional interactions present in ligand-protein frameworks, thereby deepening our comprehension of molecular mechanisms that impede the replication of bacterial cell membranes. By employing cScore, the most favorable ligand conformations of Ag–Cu/PVP-$Mg(OH)_2$ were identified within the active sites of the protein 5CPH. These were attributed to the presence of oxygen and nitrogen atoms that participate in a variety of hydrogen bond interactions with surrounding residues throughout the protein–ligand complexes, thereby markedly improving their docking scores. Fig. 8a and a′ depicts notable conformational changes within the intricate structure following the energy minimization process. PVP-$Mg(OH)_2$ had binding scores of 4.39 (Fig. 8b and b′); it is anchored to Gly85 *via* hydrogen bonding; forms an alkyl bond with Ile86; and has van der Waals interactions with Thr173, Asp81, Asn54, and Gly83. Meanwhile, Ag–Cu/PVP-$Mg(OH)_2$ is bonded to Thr173 *via* H-bonding; has van der Waals interactions with Asp81, Thr171, Arg84, Gly172, Asn54, and Gly85; and pi alkyl interactions with Arg144 and Ile86, resulting in a 6.21 binding score (Fig. 8c and c′), comparable or more significant than standard ciprofloxacin, which has a 5.98 binding score, as mentioned in Table S3 (Fig. 8d and d′).

The computational findings align closely with *in vitro* antibacterial activity, as 4% Ag–Cu/PVP-$Mg(OH)_2$ exhibited the most significant inhibition zones, measuring 5.80 ± 0.04 mm at 0.5 mg/50 μL and 7.95 ± 0.02 mm at 1.0 mg/50 μL. Meanwhile, the diminished activity of PVP-$Mg(OH)_2$ highlights the significant role of Ag–Cu in enhancing antibacterial efficacy. The enhanced binding affinity of Ag–Cu/PVP-$Mg(OH)_2$ to DNA gyrase indicates that NSs could disrupt bacterial DNA replication, thereby playing a role in its noted bactericidal effect. This offers a systematic explanation regarding the composition of materials, molecular interactions, and their biological implications.

# 4. Conclusion

In this study, $Mg(OH)_2$ and Ag–Cu/PVP-doped $Mg(OH)_2$ NSs were effectively synthesized using an environmentally benign co-precipitation technique for the removal of RhB and inhibition of bacterial growth. XRD evidenced the hexagonal phase of $Mg(OH)_2$, accompanied by an increase in crystallite size with doping. UV-Vis spectroscopy indicates the reduction in the $E_g$ from 3.5 to 2.67 eV, correlated with an increased absorption upon dopant addition. TEM revealed the formation of NRs and NSs of $Mg(OH)_2$, whereas the network of Ag–Cu NPs and $Mg(OH)_2$ NSs was observed upon doping. The interplanar spacings calculated from HR-TEM images were found to be 0.233, 0.241, 0.237, and 0.247 nm for the undoped and PVP/Au–Cu doped NSs, respectively. Among the synthesized samples, 4% Ag–Cu/PVP-$Mg(OH)_2$ showed remarkable performance, degrading 99.68% RhB in acidic medium and exhibiting a significant inhibition zone of 7.95 ± 0.02 mm for MDR *S. aureus*. The potential of the prepared NSs to inhibit *S. aureus* DNA gyrase was evaluated by employing molecular docking studies. The findings of this study reveal that the synthesized NSs are effective in degrading toxic industrial waste and

 

inhibiting pathogenic bacteria, underscoring its potential for future applications.

## Conflicts of interest

The authors declare no known conflict of interest.

## Data availability

The data used in this article are available on request.

Supplementary information is available. See DOI: https://doi.org/10.1039/d5na00693g.

## Acknowledgements

The authors are grateful to higher education commission (HEC), Pakistan, for financial support through NRPU-20-17615 (Muhammad Ikram, PI). The authors extend their appreciation to the Deanship of Research and Graduate Studies at King Khalid University for funding this work through the Large Research Project under grant number RGP2/125/46.

## References

1 K. Natarajan, H. C. Bajaj and R. J. Tayade, Photocatalytic efficiency of bismuth oxyhalide (Br, Cl and I) nanoplates for RhB dye degradation under LED irradiation, *J. Ind. Eng. Chem.*, 2016, **34**, 146–156.

2 S. Merouani, *et al.*, Sonochemical degradation of Rhodamine B in aqueous phase: effects of additives, *Chem. Eng. J.*, 2010, **158**(3), 550–557.

3 C. Lops, *et al.*, Sonophotocatalytic degradation mechanisms of Rhodamine B dye via radicals generation by micro-and nano-particles of ZnO, *Appl. Catal. B Environ.*, 2019, **243**, 629–640.

4 F. S. Mustafa and A. A. Oladipo, Rapid degradation of anionic azo dye from water using visible light-enabled binary metal-organic framework, *J. Water Proc. Eng.*, 2024, **64**, 105686.

5 Z. Wang, *et al.*, Recent advances in nanoporous membranes for water purification, *Nanomaterials*, 2018, **8**(2), 65.

6 M. Mohammed, Controlling the optical properties and analyzing mechanical, dielectric characteristics of MgO doped (PVA–PVP) blend by altering the doping content for multifunctional microelectronic devices, *Opt. Mater.*, 2022, **133**, 112916.

7 K. Naseem, *et al.*, Inorganic nanoparticles as a potential catalyst for the reduction of Rhodamine B dye: A critical review, *Inorg. Chem. Commun.*, 2024, **163**, 112367.

8 H. R. Tantawy, *et al.*, Novel synthesis of bimetallic Ag-Cu nanocatalysts for rapid oxidative and reductive degradation of anionic and cationic dyes, *Appl. Surf. Sci. Adv.*, 2021, **3**, 100056.

9 X. Liu, *et al.*, Effective destaining of methylene blue with low concentrations under visible light irradiation in the presence of Mg $(OH)_2$, *Surf. Interfaces*, 2019, **17**, 100219.

10 P. S. Das, *et al.*, Unique microstructure of 3D self-assembled Mg $(OH)_2$ nanoparticles for methylene blue degradation in presence of direct sun light, *Trans. Indian Ceram. Soc.*, 2018, **77**(4), 226–234.

11 H. R. Momenian, *et al.*, Sonochemical synthesis and photocatalytic properties of metal hydroxide and carbonate (M: Mg, Ca, Sr or Ba) nanoparticles, *J. Cluster Sci.*, 2013, **24**, 1031–1042.

12 C. Dong, *et al.*, Antibacterial study of Mg $(OH)_2$ nanoplatelets, *Mater. Res. Bull.*, 2011, **46**(4), 576–582.

13 Z. Chen, *et al.*, Adsorption-induced crystallization of U-rich nanocrystals on nano-Mg $(OH)_2$ and the aqueous uranyl enrichment, *ACS Appl. Mater. Interfaces*, 2014, **6**(2), 1301–1305.

14 C. Li, *et al.*, Recycling rare earth elements from industrial wastewater with flowerlike nano-Mg $(OH)_2$, *ACS Appl. Mater. Interfaces*, 2013, **5**(19), 9719–9725.

15 R. Bhargava and S. Khan, Effect of reduced graphene oxide (rGO) on structural, optical, and dielectric properties of Mg $(OH)_2$/rGO nanocomposites, *Adv. Powder Technol.*, 2017, **28**(11), 2812–2819.

16 K. F. Ngulube, *et al.*, Synthesis of smart ZnO@ Mg $(OH)_2$ core–shell nanocomposite and its application for methylene blue photocatalytic degradation: Life cycle sustainability assessment and techno-economics, *J. Water Proc. Eng.*, 2024, **64**, 105605.

17 K. Dharamalingam, *et al.*, Facile synthesis of polymer-based magnesium hydroxide nanocomposites for photocatalytic degradation for methylene blue dye and antibacterial application, *Biomass Convers. Biorefin.*, 2023, **13**(15), 13539–13552.

18 D. J. Calderón, *et al.*, Effect of synthesis variables on the characteristics of magnesium hydroxide nanoparticles and evaluation of the fluorescence of functionalised Mg $(OH)_2$ nanoparticles, *Adv. Nat. Sci.:Nanosci. Nanotechnol.*, 2020, **11**(2), 025008.

19 T. Saeed, *et al.*, Comparative study for removal of cationic dye from aqueous solutions by manganese oxide and manganese oxide composite, *Int. J. Environ. Sci. Technol.*, 2021, **18**, 659–672.

20 A. Alsbaiee, *et al.*, Rapid removal of organic micropollutants from water by a porous β-cyclodextrin polymer, *Nature*, 2016, **529**(7585), 190–194.

21 S. Singh, H. Mahalingam and P. K. Singh, Polymer-supported titanium dioxide photocatalysts for environmental remediation: A review, *Appl. Catal., A*, 2013, **462**, 178–195.

22 R. Dhir, Photocatalytic degradation of methyl orange dye under UV irradiation in the presence of synthesized PVP capped pure and gadolinium doped ZnO nanoparticles, *Chem. Phys. Lett.*, 2020, **746**, 137302.

23 R. Ebrahimi, *et al.*, Effects of doping zinc oxide nanoparticles with transition metals (Ag, Cu, Mn) on photocatalytic degradation of Direct Blue 15 dye under UV and visible light irradiation, *J. Environ. Health Sci. Eng.*, 2019, **17**, 479–492.

24 M. Sathishkumar, M. Saroja and M. Venkatachalam, Influence of (Cu, Al) doping concentration on the structural, optical and antimicrobial activity of ZnS thin films prepared by Sol-Gel dip coating techniques, *Optik*, 2019, **182**, 774–785.
25 O. N. Hussein, S. M. Al-Jawad and N. J. Imran, Efficient antibacterial activity enhancement in Fe/Mn co-doped CuS nanoflowers and nanosponges, *Bull. Mater. Sci.*, 2023, **46**(3), 139.
26 P. Panchal, *et al.*, Eco-friendly synthesis of Ag-doped ZnO/MgO as a potential photocatalyst for antimicrobial and dye degradation applications, *Coord. Chem. Rev.*, 2023, **493**, 215283.
27 S. S. Wagh, *et al.*, Comparative studies on synthesis, characterization and photocatalytic activity of Ag doped ZnO nanoparticles, *ACS Omega*, 2023, **8**(8), 7779–7790.
28 C. Egbuna, Preparation of bio-synthesized Ag nanoparticles and assessment of their antidiabetic and antioxidant potential against STZ-induced diabetic albino rats, *J. Biomater. Sci. Polym. Ed.*, 2024, **35**(4), 535.
29 M. F. Al-Hakkani, Biogenic copper nanoparticles and their applications: A review, *SN Appl. Sci.*, 2020, **2**(3), 505.
30 H. Bareke and A. A. Oladipo, Antimicrobial activity of biogenic-synthesized novel bimetallic nanospinel LiCu-ferrite particles: experimental and computational studies, *J. Mol. Struct.*, 2024, **1296**, 136823.
31 A. O. Ifebajo, A. A. Oladipo and M. Gazi, Sun-light driven enhanced azo dye decontamination from aqueous solution by CoO-$CuFe_2O_4$ derived from layered double hydroxide, *Desalination Water Treat.*, 2020, **177**, 423–430.
32 M. Kushwah, *et al.*, Biosynthesis of novel Ag@ Cu alloy NPs for enhancement of methylene blue photocatalytic activity and antibacterial activity, *Mater. Res. Express*, 2019, **6**(11), 116561.
33 A. Verma, *et al.*, Visible light enhanced p-nitrophenol reduction by glycerol over Ag/Cu core-shell bimetallic nanocatalysts, *J. Environ. Chem. Eng.*, 2021, **9**(4), 105655.
34 A. Hussain, *et al.*, Synergistic effect of samarium and PVP doped MgO nanostructures for RhB degradation and inhibition of DNA gyrase with molecular docking studies, *Inorg. Chem. Commun.*, 2024, **170**, 113235.
35 A. Haider, *et al.*, Green synthesized phytochemically (Zingiber officinale and Allium sativum) reduced nickel oxide nanoparticles confirmed bactericidal and catalytic potential, *Nanoscale Res. Lett.*, 2020, **15**, 1–11.
36 M. F. Mesleh, *et al.*, Fragment-based discovery of DNA gyrase inhibitors targeting the ATPase subunit of GyrB, *Bioorg. Med. Chem. Lett.*, 2016, **26**(4), 1314–1318.
37 K. Rehman, *et al.*, Taxifolin prevents postprandial hyperglycemia by regulating the activity of α-amylase: Evidence from an in vivo and in silico studies, *J. Cell. Biochem.*, 2019, **120**(1), 425–438.
38 I. Shahzadi, *et al.*, Synthesis of curcuma longa doped cellulose grafted hydrogel for catalysis, bactericidial and insilico molecular docking analysis, *Int. J. Biol. Macromol.*, 2023, **253**, 126827.
39 N. Vijaya, *et al.*, Proton conducting polymer electrolyte based on poly (N-vinyl pyrrolidone) doped with ammonium iodide, *Int. J. Electroactive Mater.*, 2015, **3**, 20–27.
40 S. Senthil, *et al.*, Enrichment of optical, magnetic and photocatalytic properties in PVP capped CdO/$SnO_2$ nanocomposites synthesized by microwave irradiation method, *J. Mater. Sci.: Mater. Electron.*, 2019, **30**, 19841–19853.
41 S. S. Mani, *et al.*, Bimetallic and plasmonic Ag and Cu integrated $TiO_2$ thin films for enhanced solar hydrogen production in direct sunlight, *Energy Adv.*, 2024, **3**(4), 829–840.
42 A. Gnanaprakasam, V. Sivakumar and M. Thirumarimurugan, A study on Cu and Ag doped ZnO nanoparticles for the photocatalytic degradation of brilliant green dye: synthesis and characterization, *Water Sci. Technol.*, 2016, **74**(6), 1426–1435.
43 P. Tzevelekidis, *et al.*, Visible-light-activated antibacterial and antipollutant properties of biocompatible Cu-doped and Ag-decorated $TiO_2$ nanoparticles, *Heliyon*, 2024, **10**(17), e35634.
44 S. Yousefi, *et al.*, Optical properties of MgO and Mg $(OH)_2$ nanostructures synthesized by a chemical precipitation method using impure brine, *J. Alloys Compd.*, 2017, **711**, 521–529.
45 S.-Y. Wang, *et al.*, Facile preparation and application of magnesium hydroxide assembly spheres, *Res. Chem. Intermed.*, 2016, **42**, 2661–2668.
46 A. Arshad, *et al.*, Graphene nanoplatelets induced tailoring in photocatalytic activity and antibacterial characteristics of MgO/graphene nanoplatelets nanocomposites, *J. Appl. Phys.*, 2017, **121**(2), 024901.
47 G. H. Jaffari, *et al.*, Study of surface-active modes and defects in single-phase Li-incorporated MgO nanoparticles, *Phys. Chem. C*, 2015, **119**(50), 28182–28189.
48 E. R. Essien, *et al.*, Biogenic synthesis of magnesium oxide nanoparticles using Manihot esculenta (Crantz) leaf extract, *Int. Nano Lett.*, 2020, **10**(1), 43–48.
49 H. Liu, *et al.*, Hydrothermal synthesis of monodisperse Ag2Se nanoparticles in the presence of PVP and KI and their application as oligonucleotide labels, *J. Mater. Chem.*, 2008, **18**(22), 2573–2580.
50 K. M. Koczkur, *et al.*, Polyvinylpyrrolidone (PVP) in nanoparticle synthesis, *Dalton Trans.*, 2015, **44**(41), 17883–17905.
51 E. M. Abdelrazek, *et al.*, Structural, optical, morphological and thermal properties of PEO/PVP blend containing different concentrations of biosynthesized Au nanoparticles, *J. Mater. Res. Technol.*, 2018, **7**(4), 419–431.
52 S. M. Briffa, *et al.*, Development of scalable and versatile nanomaterial libraries for nanosafety studies: polyvinylpyrrolidone (PVP) capped metal oxide nanoparticles, *RSC Adv.*, 2017, **7**(7), 3894–3906.
53 O. Zakir, *et al.*, Fabrication and characterization of Ag-and Cu-doped $TiO_2$ nanotubes (NTs) by in situ anodization method as an efficient photocatalyst, *J. Solid State Electrochem.*, 2022, **26**(10), 2247–2260.

54 M. Althobaiti, *et al.*, Impact of silver/copper dual-doping on the structure, linear and non-linear optical performance of ZnO thin films, *Appl. Phys. A*, 2022, **128**(6), 539.
55 R. Al-Gaashani, *et al.*, Investigation of the optical properties of Mg $(OH)_2$ and MgO nanostructures obtained by microwave-assisted methods, *J. Alloys Compd.*, 2012, **521**, 71–76.
56 P. Kaur, *et al.*, Comprehensive analysis of crystal structure, optical and luminescent behavior of Fe doped MgO nanophosphors, *Optik*, 2020, **219**, 164742.
57 W. Ahmad, *et al.*, Efficient dye degradation and antimicrobial behavior with molecular docking performance of silver and polyvinylpyrrolidone-doped Zn-Fe layered double hydroxide, *ACS Omega*, 2024, **9**(4), 5068–5079.
58 M. Alqadi, *et al.*, Influence of (Ag–Cu) co-doping on the optical, structural, electrical, and morphological properties of ZnO thin films, *J. Sol-Gel Sci. Technol.*, 2022, **103**(2), 319–334.
59 K. Sreekanth, *et al.*, Thermal, structural, optical and electrical conductivity studies of pure and $Fe^{3+}$ ions doped PVP films for semoconducting polymer devices, *Mater. Res. Innovations*, 2021, **25**(2), 95–103.
60 A. Hernández-Ramírez and I. Medina-Ramírez, *Photocatalytic Semiconductors*, Springer International Publishing, Cham, 2015.
61 B. Kulyk, *et al.*, Influence of Ag, Cu dopants on the second and third harmonic response of ZnO films, *J. Alloys Compd.*, 2009, **481**(1–2), 819–825.
62 K. Naseem, *et al.*, Inorganic nanoparticles as a potential catalyst for the reduction of rhodamine B dye: a critical review, *Inorg. Chem. Commun.*, 2024, 112367.
63 T. B. Nguyen, C. Huang and R. A. Doong, Enhanced catalytic reduction of nitrophenols by sodium borohydride over highly recyclable Au@ graphitic carbon nitride nanocomposites, *Appl. Catal. B Environ.*, 2019, **240**, 337–347.
64 A. Akbari, Membrane capsules with hierarchical Mg $(OH)_2$ nanostructures as novel adsorbents for dyeing wastewater treatment in carpet industries, *J. Taiwan Inst. Chem. Eng.*, 2017, **70**, 391–400.
65 H. A. Mohammed, *et al.*, MgO/Ni nanocomposite and its PVP-modified derivative for catalytic $CO_2$ methanation and photocatalytic hydrogen production, *Surf. Interfaces*, 2024, **51**, 104643.
66 S. Li, *et al.*, Facile synthesis of bimetallic Ag-Cu nanoparticles for colorimetric detection of mercury ion and catalysis, *Sens. Actuators, B*, 2018, **255**, 1471–1481.
67 A. Fairuzi, *et al.*, Degradation of methylene blue using silver nanoparticles synthesized from imperata cylindrica aqueous extract, in *IOP Conference Series: Earth and Environmental Science*, IOP Publishing, 2018.
68 H.-J. Cui, *et al.*, Decolorization of RhB dye by manganese oxides: effect of crystal type and solution pH, *Geochem. Trans.*, 2015, **16**, 1–8.
69 F. Chen, *et al.*, Hierarchical assembly of graphene-bridged $Ag_3PO_4$/Ag/$BiVO_4$ (040) Z-scheme photocatalyst: an efficient, sustainable and heterogeneous catalyst with enhanced visible-light photoactivity towards tetracycline degradation under visible light irradiation, *Appl. Catal. B Environ.*, 2017, **200**(330), e342.
70 C. Gong, *et al.*, Heterogeneous activation of peroxymonosulfate by Fe-Co layered doubled hydroxide for efficient catalytic degradation of Rhoadmine B, *Chem. Eng. J.*, 2017, **321**, 222–232.
71 K. Wang, *et al.*, Highly efficient photodegradation of RhB–MO mixture dye wastewater by $Ag_3PO_4$ dodecahedrons under acidic condition, *J. Mol. Catal. A: Chem.*, 2014, **393**, 302–308.
72 B. Vatsha, *et al.*, Effects of precipitation temperature on nanoparticle surface area and antibacterial behaviour of Mg $(OH)_2$ and MgO nanoparticles, *J. Biomaterials Nanobiotechnol.*, 2013, **4**(4), 365–373.
73 A. M. Azzam, *et al.*, Hexagonal Mg $(OH)_2$ nanosheets as antibacterial agent for treating contaminated water sources, *ChemistrySelect*, 2017, **2**(35), 11431–11437.
74 D. Kasai, *et al.*, An investigation into the influence of filler Piper nigrum leaves extract on physicochemical and antimicrobial properties of chitosan/poly (vinyl alcohol) blend films, *J. Polym. Environ.*, 2019, **27**, 472–488.
75 S. Kamonwannasit, *et al.*, Synthesis of copper-silver doped hydroxyapatite via ultrasonic coupled sol-gel techniques: structural and antibacterial studies, *J. Sol-Gel Sci. Technol.*, 2020, **96**, 452–463.
76 W. Fang, *et al.*, Fabrication of Cu–Ag bimetal nanotube-based copper silicates for enhancement of antibacterial activities, *RSC Adv.*, 2015, **5**(49), 39612–39619.